

Pressure-Induced Void and Crack Closure Improves the Photoconversion Efficiency and Stability of Perovskite Solar Cells

Deborah Oyewole

Worcester Polytechnic Institute

Oluwaseun Oyewole

Worcester Polytechnic Institute

Benjamin Agyei-Tuffour

University of Ghana

Juan Hinojosa Tamayo

Worcester Polytechnic Institute

Richard Koech

Worcester Polytechnic Institute

Omolara Oyelade

African Institute of Science and Technology

Sharafadeen Adeniji

Worcester Polytechnic Institute

Reisya Ichwani

Worcester Polytechnic Institute

Jaya Cromwell

Worcester Polytechnic Institute

Ridwan Ahmed

Worcester Polytechnic Institute

Erika Colin Ulloa

Worcester Polytechnic Institute

Lyubov Titova

Worcester Polytechnic Institute

Nancy Burnham

Worcester Polytechnic Institute

Winston Soboyejo (✉ wsoboyejo@wpi.edu)

Worcester Polytechnic Institute

Keywords: Applied pressure, boundary grain voids, pressure-induced void closure, power conversion efficiency, stability

Posted Date: December 30th, 2020

DOI: <https://doi.org/10.21203/rs.3.rs-134394/v1>

License:  This work is licensed under a Creative Commons Attribution 4.0 International License.

[Read Full License](#)

Abstract

One route to a brighter global energy future may be through enhancing the efficiency and stability of perovskite solar cells (PSCs), which depends on the level of defects in the photoactive absorber and along the interfaces of the multilayered structure. Here, we use a combined experimental and theoretical approach to study the effects of pressure-induced compaction of microvoids and closure of cracks on the power conversion efficiency (PCEs) and stability of formamidinium-rich PSCs. A range of mechanical pressures was applied to the PSCs to reduce pre-existing grain-boundary voids and interfacial cracks within the devices. The PCEs of the PSCs increased from $\sim 19.5\%$ to $\sim 23.5\%$ for applied pressures between $\sim (0 - 7)$ MPa. Unlaminated device stability increased by 33%, falling to 80% of initial PCE in 1800 hrs without compression, as compared to 2400 hrs with compression. The implications of this study are discussed in light of possible future manufacturing processes.

1. Introduction

Photovoltaics could contribute as much as 10 TW of power to the global energy grid by 2030¹. A candidate photovoltaic device to fulfill global demand is based on perovskite materials. Perovskites have tunable optoelectronic properties^{2,3}, and are inexpensive to manufacture⁴. Reported power conversion efficiencies (PCEs) of perovskite solar cells (PSCs) now exceed 25%⁵. Further improvement in both the performance characteristics and the stability of PSCs is essential for their applications in power generation^{6,7}.

Most of the world-record high efficiencies of PSCs are based on formamidinium (FA)⁸. This is due to their high energy absorption over a wide spectral range⁸. So far, the improvements in the efficiencies of FA-based PSCs are a result of continuous efforts in tuning optoelectronic properties^{9,10}, film passivation^{11,12}, improving processing conditions^{13,14}, tandem technology¹⁵, and the doping of materials in electron- and hole-transporting layers^{16,17}.

The use of pressure has been shown to improve optoelectronic properties of perovskite films¹⁸⁻²¹. In particular, the application of moderate pressure, during the fabrication of PSCs, has also been shown to improve interfacial surface contacts in multilayered structures of mixed-halide methylammonium perovskite solar cells, leading to enhanced efficiencies²².

In this work, we investigate the reasons for the improved performance that is observed when moderate pressures are applied to FA-rich PSCs during their fabrication. The effects of pressure application (on defects in the multilayered structures) are characterized along with their optoelectronic properties. We find that intergrain microvoids and interfacial cracks are compacted and closed due to moderate pressure application.

Thus we achieve significant improvement in the efficiencies of the pressure-assisted devices from $\sim 19.5\text{--}23.5\%$ for applied pressures between $\sim 0\text{--}7$ MPa, as well as markedly increased solar cell stability.

The results are discussed with the objective of manufacturing highly efficient and stable perovskite solar cells, within the context of pressures applied during lamination and roll-to-roll processing.

2. Results

2.1. Moderate pressure improves device efficiency and stability

We fabricated formamidinium-rich PSC devices and applied different pressure values to compact intergrain microvoids and to close interfacial cracks. The schematics of the device architecture and procedures for pressure application are presented in Fig. 1a-c, which shows the device and polydimethylsiloxane (PDMS) anvil before pressure application (Fig. 1a), as well as during a cycle of press, hold, and lift using the PDMS anvil (Fig. 1b). The pressure – time curves are also presented in Fig. 1c for the different applied pressures.

We see an improvement in the performance characteristics of the devices as we increased the applied pressure. Figure 2a presents the current density – voltage (J-V) curves of the devices for different applied pressures. The current density significantly increased from 25.7 (23.1 ± 1.4) mA cm^{-2} to 28.3 (26.4 ± 0.9) mA cm^{-2} for applied pressures between 0 MPa and 7 MPa. Note that the data are reported in the format Best (Average \pm Standard Deviation). We also observed a decrease in the current density to 24.5 (22.7 ± 1.7) mA cm^{-2} when higher pressures of 10 MPa were applied to the devices.

The PCEs of the devices also increased from 19.5 (17.7 ± 1.6) % to 23.5 (21.6 ± 2.0) % (Fig. 2b), as we increased the applied pressures from 0 MPa to 7 MPa. At a pressure of 10 MPa, the PCE decreased to 18.8 (16.1 ± 1.7) %. Figure 2c shows the histograms of the PCEs for pressures between 0 MPa and 7 MPa, while Table 1 summarizes the results obtained from perovskite solar cells that were subjected to different applied pressures during their fabrication.

Table 1

Summary of device characteristic parameters (PCEs, J_{sc} , V_{oc} and FF) with the best, average, and standard deviation values.

Pressure (MPa)	PCE (%)	J_{sc} (mA cm ⁻²)	V_{oc} (V)	FF
0.0	19.5 (17.7 ± 1.6) ^a	25.7 (23.1 ± 1.4)	1.110 (1.057 ± 0.027)	0.690 (0.615 ± 0.044)
3.0	21.3 (20.0 ± 1.1) ^b	26.3 (25.3 ± 0.6)	1.110 (1.063 ± 0.025)	0.681 (0.616 ± 0.052)
5.0	22.4 (21.0 ± 1.8) ^c	26.7 (25.7 ± 0.6)	1.100 (1.065 ± 0.025)	0.701 (0.650 ± 0.037)
7.0	23.5 (21.6 ± 2.0) ^d	28.3 (26.4 ± 0.9)	1.121 (1.086 ± 0.028)	0.752 (0.670 ± 0.038)
10.0	18.8 (16.1 ± 1.7) ^e	24.5 (22.7 ± 1.7)	1.091 (1.042 ± 0.027)	0.657 (0.621 ± 0.027)
^a 38 devices, ^b 28 devices, ^c 27 devices, ^d 26 devices, ^e 25 devices				

To understand the mechanisms that drive the enhanced performance of the devices with increased pressure, we carried out cross-sectional SEM imaging of the devices before and after pressure application. Figure 2d-f presents the cross-sectional SEM images of the devices for the following conditions: no pressure (Fig. 2d); moderate pressure at 7 MPa (Fig. 2e), and too much of pressure at 10 MPa (Fig. 2f).

In the case of as-prepared devices (fabricated with no pressure application), a significant number of grain-boundary voids and some intergranular cracks were observed across the photoactive perovskite layer (Fig. 2d). However, after compaction, most of the voids and the intergranular cracks were fully closed in the SEM cross-sections of the devices that were fabricated with pressures of 7 MPa (Fig. 2e). However, for devices fabricated with an applied pressure of 10 MPa, we observed both interfacial cracking (at the interface between the perovskite layer and the mesoporous TiO₂ layer and the interface between the perovskite layer and the Spiro-OMeTAD layer), and grain-boundary cracking in the photoactive layer (Fig. 2f).

To explore the influence of pressure on the device stability over time, PCEs were measured under continuous 1-sun illumination for devices without pressure and those that were assisted with the optimum pressure of 7 MPa. We also studied their long-term stability by storing the devices in a desiccator (at room temperature 22-25°C and relative humidity 20–60%). We measured their performance at different times over a period of five months.

The PCEs of the devices under continuous illumination and the evolution of PCEs over the period of five months are presented in Figs. 2g and 2 h, respectively. While the optimum pressure-assisted devices have

longer stability before degrading to 80% of the initial PCEs (~ 2400 h), the as-prepared devices degrade faster to 80% of their initial PCEs within ~ 1800 h.

The histograms and Weibull distribution curves of the device PCEs are presented in Fig. 3a-e for different applied pressures. The estimated values of the PCEs, that correspond to the peaks of the Weibull curves, increased with increasing pressure (Fig. 3f). We also see an increase in the current density of the devices with increased applied pressures between 0 MPa – 7 MPa (Fig. 4a), while the Fill Factor (FF) also increased with increasing pressure (Fig. 4b). However, there is no significant increase in the open circuit voltage (Fig. 4c). We attribute the improved performance of the devices to compaction of grain-boundary voids and closure of interfacial cracks for pressures between 0 MPa to 7 MPa.

2.2. Moderate pressure closes voids and cracks

To gain more insight into the mechanics involving closing of grain-boundary voids and interfacial defects that occur during pressure application, we used the ABAQUS software package (ABAQUS, Dassault Systemes, Pawtucket, RI, USA) to simulate the effects of pressure application on multilayered PSCs structures with pre-existing interfacial defects. The models assume that, in a model PSC structure, there are pre-existing grain-boundary cracks and voids^{11,12,21,23,24}, as well as interfacial defects (voids and interfacial cracks) before pressure application (Fig. 5a). Our hypothesis is that these defects can be closed by applying moderate pressure (Fig. 5b). A representative axisymmetric model of the interfacial defects between the perovskite layer and the mesoporous-TiO₂ along with the boundary conditions is shown in Fig. 5c.

We assumed that the parts of the device that are farther from the pre-existing interfacial defects have no significant effect on the mechanics around the defect. All parts were created in Abaqus while the mechanical properties of the different materials^{25–28} were incorporated into the created sections to run the simulations. All the materials were assumed to exhibit isotropic elastic behavior.

All the parts of the model were meshed using four-node bilinear axisymmetric quadrilateral elements. We ensured that the mesh sizes were identical and dense in the regions near the pre-existing interfacial defects for convergence in the simulation. While an axisymmetric boundary condition was applied at the symmetry axis (Fig. 5c), the device substrate was fixed to have no displacements and no rotations. We also fixed the outer edge of the model to have no lateral movement for continuity. Different pressures were then applied to the device to close up interfacial defects.

We see improved interfacial contact from the devices assisted with little or no pressure (10^{-5} MPa) to high pressure of 10 MPa (Fig. 5d-f). A detailed evolution of the stress distribution in the layered structure for different applied pressures (Fig. 6) shows that the stress distribution increases with applied pressure. We find that the induced stresses along the interface and within the layered structure are more than the pressures applied remotely. The stresses are concentrated within gold and perovskite layers which are shown in Fig. 6 insets. At higher pressures, cracks can initiate from the region of high stress

concentration which is evident in the cross section SEM image at higher pressure (Fig. 2f). The results of the simulation are consistent with void and crack closure due to moderate external pressure.

2.3. Moderate pressure lowers defect density

Knowing that moderate pressure can improve interfacial contacts, we deposited the perovskite multilayer films onto FTO-coated glass slides to further study defect density as a function of applied pressure. Figure 7a-e presents the cross-sectional SEM images of the perovskite multilayers for applied pressures between 0 MPa and 10 MPa. We observed a significant decrease in grain-boundary defects or voids as the applied pressures increased from 0 MPa to 10 MPa, leading to closely packed grains that can improve both efficiency and stability of PSCs^{19,22,29}. However, we observed patches of damaged grains at the top of the perovskite films at 10 MPa (Fig. 7e). Figure 7f presents grain-boundary void areas, as determined by analysis of the SEM images using ImageJ software. The results show a significant decrease in the areas of the voids as it can be physically observed on the cross section SEM images (Fig. 7a-e).

The above results of pressure-effects on defects have significant implications for charge carrier dynamics in PSCs. Both grain-boundary and interfacial defects in PSCs can act as charge carrier traps³⁰ and recombination sites^{31,32}. Carrier trapping and defect-mediated recombination can significantly affect the optical properties of the perovskite films, which we have investigated as a function of applied pressure, using optical absorbance and photoluminescence (PL) spectra.

Both the optical absorbance and PL spectra are presented in Fig. 7g. The photon absorption increased with increasing pressure from 0 MPa to 7 MPa (Fig. 7g), and then decreased in the perovskite films prepared with applied pressures above 7 MPa (Fig. 7g inset). The increase in the peaks of the PL spectra for pressures between 0–7 MPa (Fig. 7g) is evidence of defect density reduction in the films, as the number of voids decreases with the increasing pressure. For the applied pressures beyond 7 MPa (i.e. pressure of 10 MPa), the PL intensity is reduced due to film damage (Fig. 7e). The initiation of cracking at an applied pressure of 10 MPa mitigates the transport of charge carriers within the multilayered structures of PSCs, which results ultimately in the decrease of the PCEs obtained for the devices fabricated with a pressure of 10 MPa.

Beyond examining PL spectra, Time-Resolved Photo-Luminescence (TRPL) provides an additional insights into the radiative lifetimes of the photoexcited charge carriers. TRPL decays taken at the peak of emission for early times (< 40 ns) (Fig. 8a) were analyzed by fitting them to a bimolecular function (Eq. 1).

$$I = I_0(1 + at)^{-2}, \quad (1)$$

where I , I_0 , a and t are the intensity, peak magnitude, bimolecular rate and time, respectively.

We find that application of pressure up to 7 MPa dramatically increases peak photoluminescence (Fig. 8b) while simultaneously increasing bimolecular rate (Fig. 8c). Increase in both of these parameters is indicative of the reduction in the density of deleterious defects. In agreement with structural studies that showed that increasing the pressure beyond 7 MPa to 10 MPa results in structural damage and an accompanying increase in the defect concentration, both the PL intensity and the bimolecular recombination rate exhibit a dramatic decrease in the film prepared with 10 MPa. We conclude that moderate pressure improves the carrier dynamics of multilayer perovskite films, but too much pressure is detrimental.

3. Discussion

Our study provides some new insights into the effects of pressure on the microvoid compaction and crack closure that can occur during the pressure-assisted fabrication of perovskite solar cells. Such remotely applied moderate pressures (between 0 and 7 MPa) close up cracks and voids. The closing up of the defects also reduces carrier recombination, as is evident in the photoluminescence results³³. The defect reduction in the photoactive perovskite layers and along interfaces promotes light absorption that generates more charge carriers.

Although the remote application of moderate pressure induces high stresses around grains, as established by our simulation results, it can also induce the closure of the intergranular cracks in the active perovskite layers (Fig. 2d-f). Such closure can enhance charge and light transport within the perovskite layers. It can also reduce the transport of water vapor within grain boundary and porous sections of the multilayered PSC structures.

Since such moisture can absorb to, or react with layers in the PSC structures to cause device degradation, the observed closure of grain boundary cracks (pathways for grain boundary diffusion), porosity/microvoids and interfacial cracks (pathways for enhanced internal diffusion), should lead to improved PSC stability for devices fabricated with pressures up to 7 MPa. However, for devices fabricated with pressures of 10 MPa, the induced cracks at these higher pressure levels reduce the overall levels of charge transport, while enabling enhanced charge recombination. Hence, the PCEs of the PSCs produced with applied pressures of 10 MPa are lower than those produced with applied pressures of 7 MPa.

The above insights are important for the design of pressure-assisted processes for the fabrication of perovskite solar cells. These may include: lamination processes³⁴ or roll-to-roll-processing^{35,36} that can be used to fabricate PSCs under well controlled pressure application. These fabrication processes may also be combined with encapsulation processes that limit the percolation of water vapor into the PSCs under potential service conditions. They may, therefore, enhance the stability of the PSCs, while providing future opportunity to enhance the photoconversion efficiencies that can be achieved in future pressure-assisted perovskite solar cells.

4. Conclusions

In summary, the photoconversion efficiencies of perovskite solar cells can be enhanced by applying moderate remote pressures (up to 7 MPa) during solar cell fabrication. Such pressure application leads to void compaction and crack closure. However, higher pressures degrade the device performance due to structural damage by cracking. Furthermore, devices with lower defect densities live longer under ambient conditions without any encapsulation. The benefits of moderate applied pressure can be exploited for future lamination and roll-to-roll processes in the manufacture of perovskite solar cells – for a brighter energy future.

5. Experimental Section

Materials Processing.

All materials were purchased from Sigma Aldrich. First, two different molar concentrations (0.15 M in 1-butanol and 0.3 M in 1-butanol) of titanium diisopropoxide bis (acetylacetonate) were prepared and sonicated for 30 min. A solution of mesoporous titanium oxide paste was prepared by dissolving a titania paste in ethanol (20% in ethanol) before sonicating continuously for 2 hours. A solution of lead (II) iodide (PbI_2) (> 98.9% purity, Sigma Aldrich) was also prepared from a mixture of 599.3 mg in 1 ml of DMF:DMSO (19:1, volume ratio). This was stirred continuously on a magnetic stirrer at 500 rpm for 2 hours at a constant temperature of 60 °C. The solution was then filtered through a 0.20 μm mesh filter.

Subsequently, a solution of formamidinium (FA)-rich mixed-organic halides was prepared by dissolving 60 mg of formamidinium iodide (FAI) (Sigma Aldrich), 6 mg of methylammonium bromide (MABr) (Sigma Aldrich) and 6 mg of methylammonium chloride (Sigma Aldrich) in 1 ml of isopropyl alcohol (Sigma Aldrich). The mixture was sonicated for 1 hour in an ultrasonic bath. Finally, a solution of 2,2',7,7'-tetrakis (N,N-di-p-methoxyphenylamine)-9,9'-spirobifluorene (Spiro-OMeTAD) (> 99% purity, Sigma Aldrich) was prepared by mixing 72 mg of Spiro-OMeTAD, 17.5 μl of lithium bis (trifluoromethylsulphony) imide (Li-FTSI) (Sigma Aldrich) (500 mg in 1 ml of acetonitrile), and 28.2 μl of 4-tert-butylpyridine (tBP) (Sigma Aldrich) in 1 ml of chlorobenzene.

Fabrication of Layered PSCs.

FTO-coated glass and bare glass substrates were cut into dimensions 25 mm x 25 mm and sonicated successively (each for 15 min) in decon-90 detergent, deionized water, acetone (Sigma Aldrich), and IPA (Sigma Aldrich). The cleaned substrates were then blow-dried in nitrogen gas, prior to UV-Ozone cleaning (Novascan, Main Street, Ames, IA, USA) for 20 minutes to remove organic residuals. An electron transport layer (ETL) (that comprises compact and mesoporous layers of titanium oxide) was deposited onto FTO-coated glass, following a previous protocol²².

First, a compact titanium oxide (c-TiO_2) was spin-coated onto the cleaned FTO-coated glass from the 0.15 M solution of titanium diisopropoxide bis (acetylacetonate) at 2000 rpm for 30 s. This was annealed

at 150 °C for 5 min before spin coating the 0.3 M solution of titanium diisopropoxide bis (acetylacetonate) at 2000 rpm for 30 s. The deposited c-TiO₂ was then sintered in a furnace (Lindberg Blue M, Thermo Fisher Scientific) at 500 °C for 30 minutes. The sample was allowed to cool down to room-temperature (~ 22 °C) overnight. Subsequently, a mesoporous titanium oxide (mp-TiO₂) layer was spin coated from the solution of titanium oxide paste at 5000 rpm for 30 s before sintering at 500 °C for 30 min in a furnace (Lindberg Blue M, Thermo Fisher Scientific).

A perovskite layer was deposited onto mp-TiO₂/c-TiO₂/FTO-coated and a bare glass in two steps. The solution of PbI₂ was spin-coated onto the mp-TiO₂ layer at 1500 rpm for 30 s. This was annealed at 70 °C for 1 min. The solution of FA-rich mixed-organic halides was then spin-coated onto the PbI₂ layer at 1300 rpm for 30 s. This was followed by annealing at 130 °C for 15 min before spin-coating the solution of Spiro-OMeTAD onto the perovskite layer at 5000 rpm for 30 s. It is important to note here that all layers (from c-TiO₂ to Spiro-OMeTAD) were deposited under ambient conditions (room temperature was 22–25 °C and relative humidity was 20–60%). Finally a 80.0 nm thick gold (Au) layer was thermally evaporated onto the Spiro-OMeTAD layer using an Edward E306A evaporation system (Edward E306A, Easton PA, USA). The evaporation was carried out under a vacuum pressure of ~ 1.0 × 10⁻⁶ Torr at a deposition rate of 0.15 nm s⁻¹.

Pressure Experiments.

To improve interfacial surface contacts and to heal grain-boundary defects, a range of pressures (0–10 MPa) was applied to the perovskite multilayers and the fabricated perovskite solar cells. A MicroTester Instron machine (MicroTester, Instron 5848, Norwood, MA, USA) was used with a PDMS anvil that protects the device. First, the PDMS anvil was fabricated from a mixture of Sylgard 184 silicone elastomer base and Sylgard 184 silicone elastomer curing agent (Dow Corning Corporation, Midland, MI) in a ratio 10:1 by weight. The mixture was degassed and cured (at 65 °C for 2 hours) in a mold with polished silicon base.

The PDMS anvil was then cut out into the dimensions of the device's glass substrate and attached to the crosshead of the Instron machine with the surface that was cured against the polished silicon facing down. A schematic of the set-up before the ramping of the head of Instron is shown in Fig. 1a. The Instron was set to ramp in compression at a displacement rate of 1.0 mm min⁻¹ to press and hold down the device (Fig. 1b) at 3 MPa for 5 minutes. Unloading was then carried out at a displacement rate of ~ 1.0 mm min⁻¹. This was then repeated for different peak pressures (from 3 MPa to 10 MPa) on the PSCs and perovskite layers. The pressure – time curves that show the regions of loading, holding, and unloading are presented in Fig. 1c.

Characterization of Layered PSCs.

The optical absorbances of the multilayer films were measured using an Avantes UV-Vis spectrophotometer (AvaSpec-2048, Avantes, BV, USA). The PL and TRPL measurements were obtained by exciting the films with a 405 nm picosecond laser source (Aura Technology PIXEA) using 270 nW incident power, 2 kHz repetition rate and 50% of tuning. The excitation signal was sent to a Horiba MicOS microscope optical spectrometer system that consists of a Horiba iHR550 spectrometer, a luminescence microscope with a 50X Edmund Optics Plan Apo NIR Mitutoyo objective, and a Horiba Synapse EM CCD camera. The PL spectra and TRPL measurements were then obtained using a single photon counter module (SPD-OEM-VIS, Aurea Technology) and an acquisition software interface.

The microstructures of perovskite films and the cross section of PSCs were obtained using a field-emission scanning electron microscope (SEM) (JEOL JSM-700F, Hollingsworth & Vose, MA, USA) with an SEM working distance of 10–11 mm at a low accelerating voltage of 5 kV. Current density against voltage (J-V) were measured (before and after the pressure treatment) using a Keithley source meter unit (SMU2400) (Keithley, Tektronix, Newark, NJ, USA) that was connected to an Oriel solar simulator (Oriel, Newport Corporation, Irvine, CA, USA) under AM1.5G illumination of 90 mW cm^{-2} . The SMU was operated using a KickStart instrument control software. The solar simulator was calibrated using a 918D high performance calibrated photodiode sensor (Newport). The device was masked to expose an area of 0.13 cm^2 to illumination.

Declarations

Data availability

The authors declare that the data supporting the findings of this study are available within the paper

Acknowledgements

The authors are grateful to the World Bank (Pan African Materials Institute supported by the World Bank African Centers of Excellence Program – Grant No: P126974) and the Worcester Polytechnic Institute for financial support.

Author Contributions

W. O. S. conceived the idea, O. K. O., D. O. O. and B. A. fabricated and characterized different layers of all devices, O. K. O., D. O. O., R. K. K., R. I., J. C., R. A. and B. A. carried out all microstructural imaging, optical and XRD measurements, E.C.U and L. V. T. carried out all photoluminescence measurements, W. O. S., O. K. O., J. H. and N. B. analyzed the defects, O. K. O. and D. O. O. wrote the manuscript, S. A. A., V. O. O., L. V. T., B. A., N. A. B. and W. O. S. revised the manuscript.

Competing Interests

The authors declare no conflicts of interests.

References

1. Haegel, N. M. *et al.* Terawatt-scale photovoltaics: Transform global energy. *Science* **364**, 836-838 (2019).
2. Chouhan, L., Ghimire, S., Subrahmanyam, C., Miyasaka, T. & Biju, V. Synthesis, optoelectronic properties and applications of halide perovskites. *Chemical Society Reviews* **49**, 2869-2885 (2020).
3. Song, T. *et al.* Perovskite solar cells: film formation and properties. *J. Mater. Chem. A* **3**, 9032-9050 (2015).
4. Snaith, H. Perovskites: The Emergence of a New Era for Low-Cost. *High-Efficiency Sol.* **4**, 3623-3630 (2013).
5. NREL. National Renewable Energy Laboratory Photovoltaic Research: Best Research-Cell Efficiency Chart. *Best Research-Cell Efficiency Chart | Photovoltaic Research | NREL* (2020).
6. Leijtens, T. *et al.* Stability of metal halide perovskite solar cells. *Adv. Energy Mater.* **5**, 1500963; [10.1002/aenm.201500963](https://doi.org/10.1002/aenm.201500963) (2015).
7. Correa-Baena, J. P. *et al.* Promises and challenges of perovskite solar cells. *Science* **358**, 739-744 (2017).
8. Han, Q. *et al.* Single Crystal Formamidinium Lead Iodide (FAPbI₃): Insight into the Structural, Optical, and Electrical Properties. *Adv. Mater.* **28**, 2253-2258 (2016).
9. Zhang, S. *et al.* Formamidinium-assisted fast crystallization to fabricate formamidinium-based perovskite films for high-efficiency and stable solar cells. *J. Mater. Chem. C* **8**, 1642-1648 (2020).
10. Rahmany, S., Rai, M., Gutkin, V., Wierzbowska, M. & Etgar, L. Tuning the Optical Properties of Already Crystallized Hybrid Perovskite. *Sol. RRL* **3**, 1900128; [10.1002/solr.201900128](https://doi.org/10.1002/solr.201900128) (2019).
11. Qian, F. *et al.* Novel Surface Passivation for Stable FA0.85MA0.15PbI₃ Perovskite Solar Cells with 21.6% Efficiency. *Sol. RRL* **3**, 1900072; [10.1002/solr.201900072](https://doi.org/10.1002/solr.201900072) (2019).
12. Lee, D. S. *et al.* Passivation of Grain Boundaries by Phenethylammonium in Formamidinium-Methylammonium Lead Halide Perovskite Solar Cells. *ACS Energy Lett.* **3**, 647-654 (2018).
13. Fan, Y., Meng, H., Wang, L. & Pang, S. Review of Stability Enhancement for Formamidinium-Based Perovskites. *Solar RRL* **3**, 1900215; [10.1002/solr.201900215](https://doi.org/10.1002/solr.201900215) (2019).
14. Min, H. *et al.* Efficient, stable solar cells by using inherent bandgap of a-phase formamidinium lead iodide. *Science* **366**, 749-753 (2019).
15. Bush, K. A. *et al.* 23.6%-efficient monolithic perovskite/silicon tandem solar cells with improved stability. *Nat. Energy* **2**, 17009; [10.1038/nenergy.2017.9](https://doi.org/10.1038/nenergy.2017.9) (2017).
16. Jeong, J. *et al.* Formamidinium-based planar heterojunction perovskite solar cells with alkali carbonate-doped zinc oxide layer. *RSC Adv.* **8**, 24110-24115 (2018).

17. Geffroy, C. *et al.* p-Doping of a Hole Transport Material via a Poly(ionic liquid) for over 20% Efficiency and Hysteresis-Free Perovskite Solar Cells. *ACS Appl. Energy Mater.* **3**, 1393–1401 (2020).
18. Shi, L. *et al.* Effect of Pressing Pressure on the Performance of Perovskite Solar Cells. *ACS Appl. Energy Mater.* **2**, 2358–2363 (2019).
19. Ghosh, D., Aziz, A., Dawson, J. A., Walker, A. B. & Islam, M. S. Putting the Squeeze on Lead Iodide Perovskites: Pressure-Induced Effects to Tune Their Structural and Optoelectronic Behavior. *Chem. Mater.* **31**, 4063–4071 (2019).
20. Zhang, L., Wang, L., Wang, K. & Zou, B. Pressure-Induced Structural Evolution and Optical Properties of Metal-Halide Perovskite CsPbCl₃. *J. Phys. Chem. C* **122**, 15220–15225 (2018).
21. Han, T. H. *et al.* Interface and Defect Engineering for Metal Halide Perovskite Optoelectronic Devices. *Advanced Materials* **31**, 1803515 (2019) doi:10.1002/adma.201803515.
22. Oyelade, O. V. *et al.* Pressure-Assisted Fabrication of Perovskite Solar Cells. *Sci. Rep.* **10**, 7183; 10.1038/s41598-020-64090-5 (2020).
23. Wang, F., Bai, S., Tress, W., Hagfeldt, A. & Gao, F. Defects engineering for high-performance perovskite solar cells. *npj Flexible Electronics* **22**, 1; 10.1038/s41528-018-0035-z (2018).
24. Wang, Y. *et al.* Comprehensive Elucidation of Grain Boundary Behavior in All-Inorganic Halide Perovskites by Scanning Probe Microscopy. *Adv. Mater. Interfaces* **7**, 1–8 (2020).
25. Sun, S., Fang, Y., Kieslich, G., White, T. J. & Cheetham, A. K. Mechanical properties of organic-inorganic halide perovskites, CH₃NH₃PbX₃ (X = I, Br and Cl), by nanoindentation. *J. Mater. Chem. A* **3**, 18450–18455 (2015).
26. Feng, J. Mechanical properties of hybrid organic-inorganic CH₃NH₃BX₃ (B = Sn, Pb; X = Br, I) perovskites for solar cell absorbers. *APL Mater.* **2**, 081801; 10.1063/1.4885256 (2014).
27. Park, M. *et al.* Mechanically Recoverable and Highly Efficient Perovskite Solar Cells: Investigation of Intrinsic Flexibility of Organic-Inorganic Perovskite. *Adv. Energy Mater.* **5**, 1–11 (2015).
28. Reyes-Martinez, M. A. *et al.* Time-Dependent Mechanical Response of APbX₃ (A = Cs, CH₃NH₃; X = I, Br) Single Crystals. *Adv. Mater.* **29**, 1–7 (2017).
29. Lü, X., Yang, W., Jia, Q. & Xu, H. Pressure-induced dramatic changes in organic-inorganic halide perovskites. *Chem. Sci.* **8**, 6764–6776 (2017).
30. Li, W., Long, R., Tang, J. & Prezhdov, O. V. Influence of Defects on Excited-State Dynamics in Lead Halide Perovskites: Time-Domain *ab Initio* Studies. *J. Phys. Chem. Lett.* **10**, 3788–3804 (2019).
31. Sherkar, T. S. *et al.* Recombination in Perovskite Solar Cells: Significance of Grain Boundaries, Interface Traps, and Defect Ions. *ACS Energy Lett.* **2**, 1214–1222 (2017).
32. Ball, J. M. & Petrozza, A. Defects in perovskite-halides and their effects in solar cells. *Nat. Energy* **1**, 16149; 10.1038/nenergy.2016.149 (2016).
33. Phung, N. *et al.* The Role of Grain Boundaries on Ionic Defect Migration in Metal Halide Perovskites. *Adv. Energy Mater.* **10**, 1903735; 10.1002/aenm.201903735 (2020).

34. Schmager, R. *et al.* Laminated Perovskite Photovoltaics: Enabling Novel Layer Combinations and Device Architectures. *Adv. Funct. Mater.* **30**, 1907481; 10.1002/adfm.201907481 (2020).
35. Kim, Y. Y. *et al.* Roll-to-roll gravure-printed flexible perovskite solar cells using eco-friendly antisolvent bathing with wide processing window. *Nat. Commun.* **11**, 5156; 10.1038/s41467-020-18940-5 (2020).
36. Kim, Y. Y. *et al.* Gravure-Printed Flexible Perovskite Solar Cells: Toward Roll-to-Roll Manufacturing. *Adv. Sci.* **6**, 1802094; 10.1002/advs.201802094 (2019).

Figures

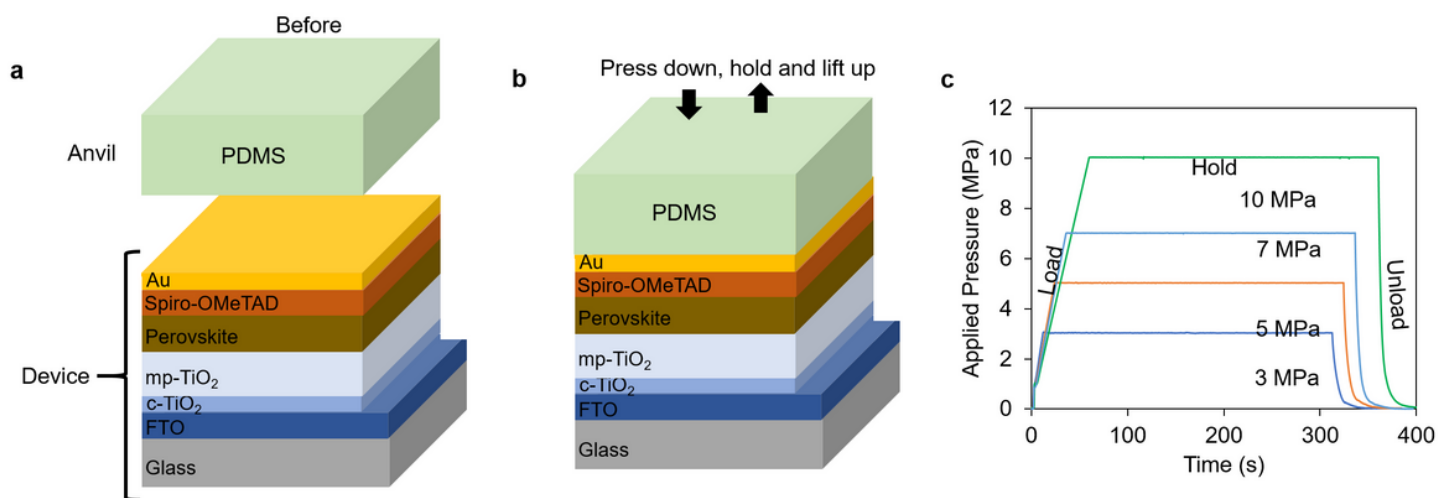


Figure 1

Schematics of device architecture and procedure for pressure application as well as pressure – time curves. (a) Schematic of device architecture and polydimethyl siloxane (PDMS) stamp before pressure application. (b) Schematic of the perovskite device being assisted with pressure by pressing, holding down, and lifting up of the PDMS stamp. (c) Pressure – time curves for applied pressures 3, 5, 7, 10 MPa which show load, hold, and unload regions.

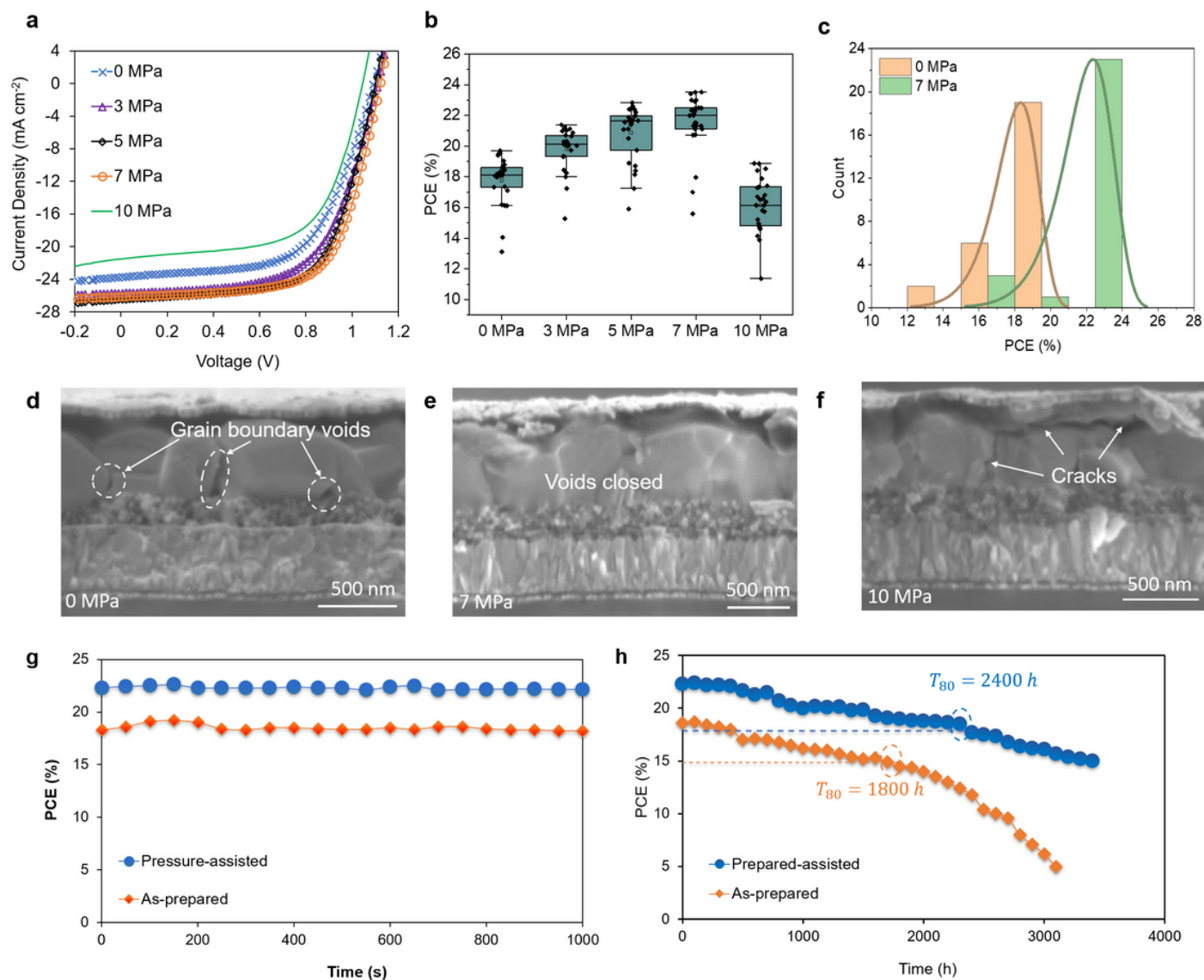


Figure 2

Electrical properties and cross section SEM images of devices. (a) Current density – voltage curves of perovskite solar cells that were assisted with different applied pressures: 0, 3, 5, 7 and 10 MPa. (b) Box-and-whisker plot of the device PCEs at the different applied pressures. (c) Histograms of the PCEs of the devices assisted with 0 MPa and 7 MPa pressures. (d-f) Typical SEM images of the device cross sections which show grain-boundary voids/defects in d, compact grains in e and cracking in f. (g) Steady-state PCE under continuous 1-sun illumination for as-prepared and pressure-assisted devices. (h) Evolution of device PCEs over a period of five months; devices were kept in a desiccator under room temperature (22 – 25 °C) and relative humidity (20 – 60 %). A pressure of 7 MPa optimizes both the PCE and stability.

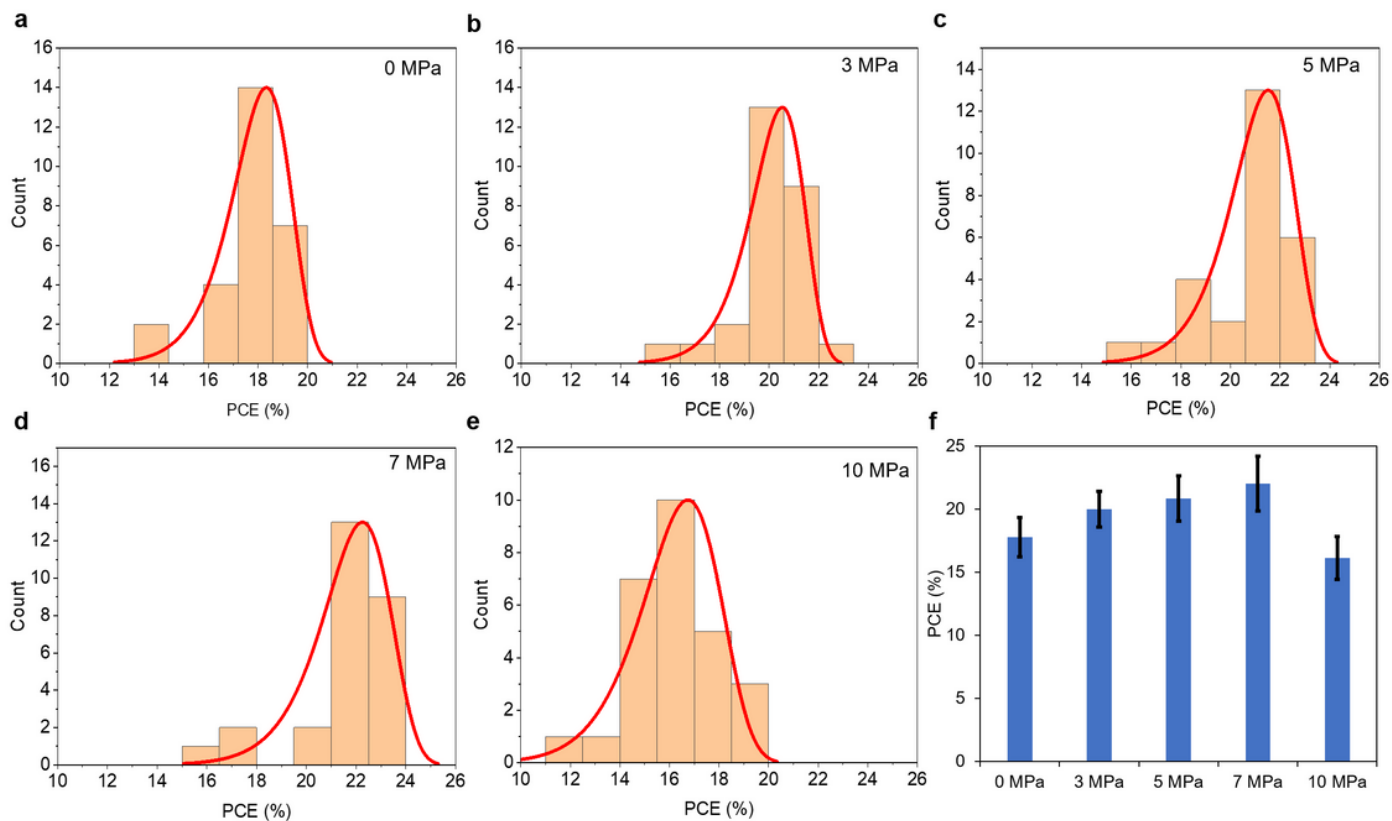


Figure 3

Power conversion efficiencies (PCEs) of PSC devices for different applied pressures: (a-e) Histogram of PCEs of devices and the distribution curves for 0, 3, 5, 7, and 10 MPa applied pressures. (f) Summary of the PCEs for different applied pressures. The highest PCE occurs at the optimal pressure of 7 MPa.

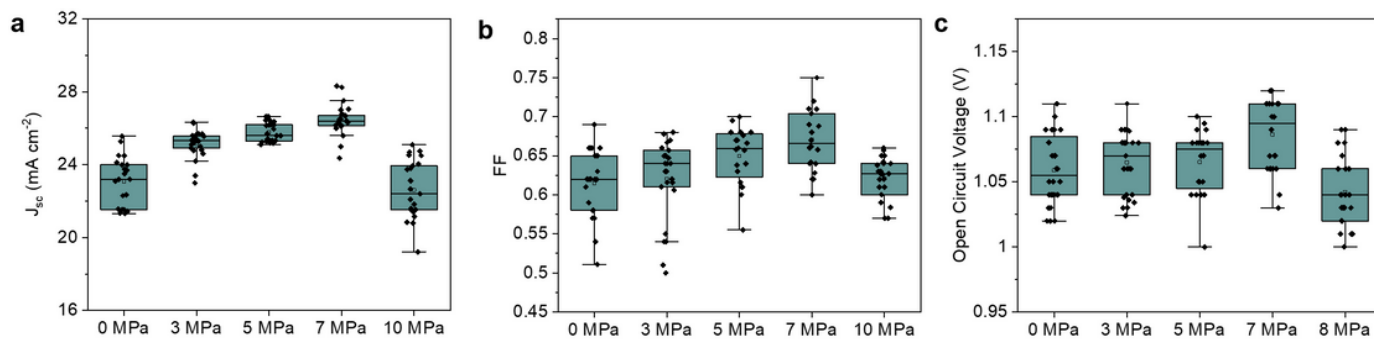


Figure 4

Evolution of parameters of pressure-assisted device: (a) Short circuit current-densities (J_{sc}) of devices that show a increase in the J_{sc} for pressures between 3 – 7 MPa. (b) Fill factor (FF) as a function of the applied pressure, showing an increased FF for increasing pressure up to 7 MPa before a decrease at 10 MPa. (c) Open circuit voltages (V_{oc}) of devices, with no significant change in the V_{oc} . At 7 MPa, the

current density is high and the fill factor at its maximum, leading to the highest values of PCE at this pressure.

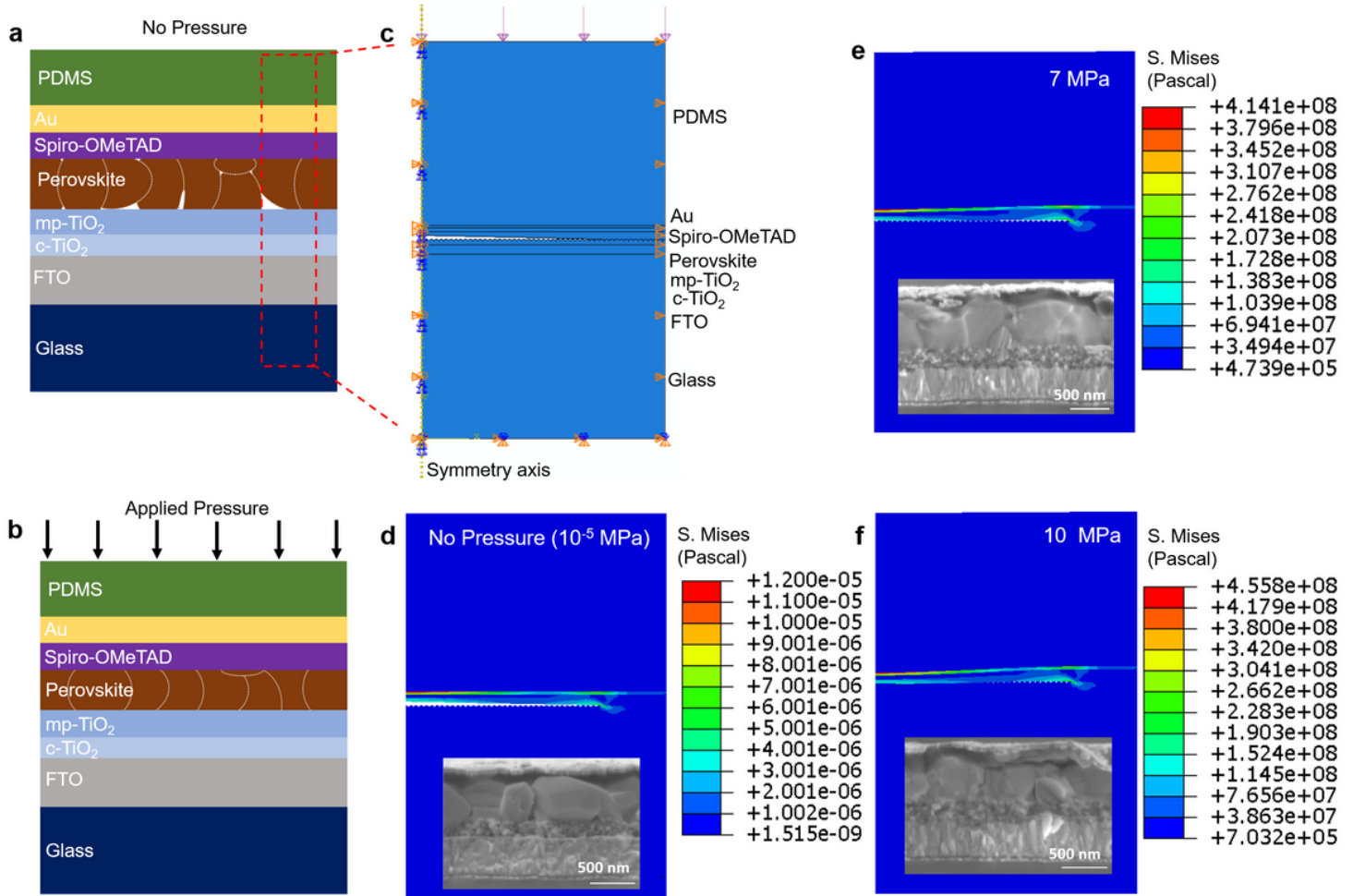


Figure 5

Computational modeling of interfacial defects in PSCs. (a) A schematic of the no-pressure PSC that shows idealized pre-existing grain-boundary and interfacial defects. (b) A schematic of the pressure-assisted PSC which depicts closing of the idealized pre-existing defects. (c) Model developed with Abaqus software. (d-f) Von-Mises stress distribution in the PSCs for applied pressures: 10⁻⁵ MPa (no pressure), 7 MPa, and 10 MPa; we used 10⁻⁵ MPa for the no-pressure device since our model cannot run with load of 0 MPa. Insets in d-f are the cross-sectional SEM images. The as-fabricated devices have voids, which are compacted by moderate pressure. Too much pressure, however, creates cracks.

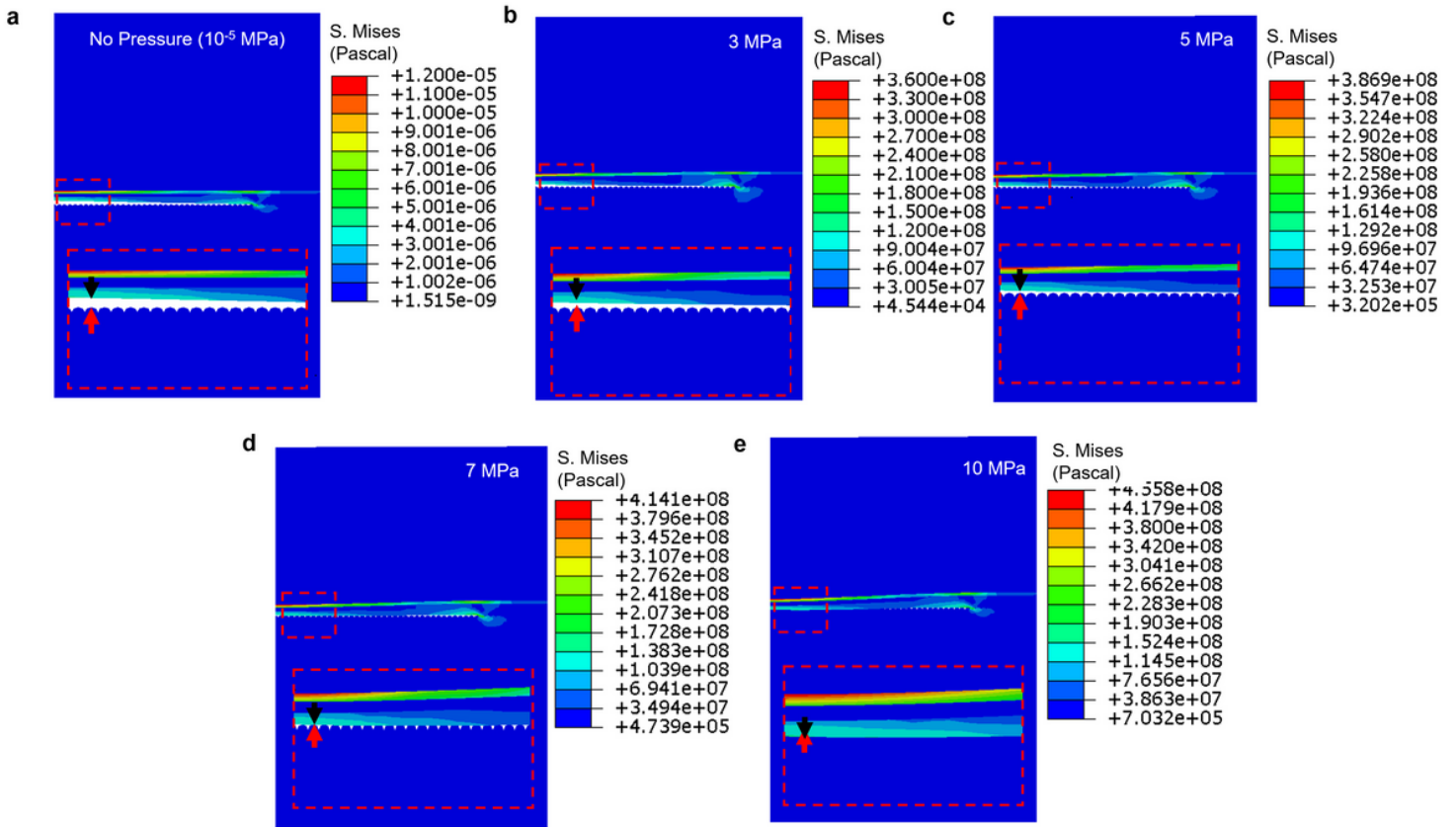


Figure 6

Von-Mises stress distribution in layered PSCs for the different applied pressures: (a) 10^{-5} MPa (no pressure), (b) 3 MPa, (c) 5 MPa, (d) 7 MPa and (e) 10 MPa. As stress increases, the size of the interfacial defect decreases with increasing applied pressure. Displacement of materials for the closure of void is indicated by arrows.

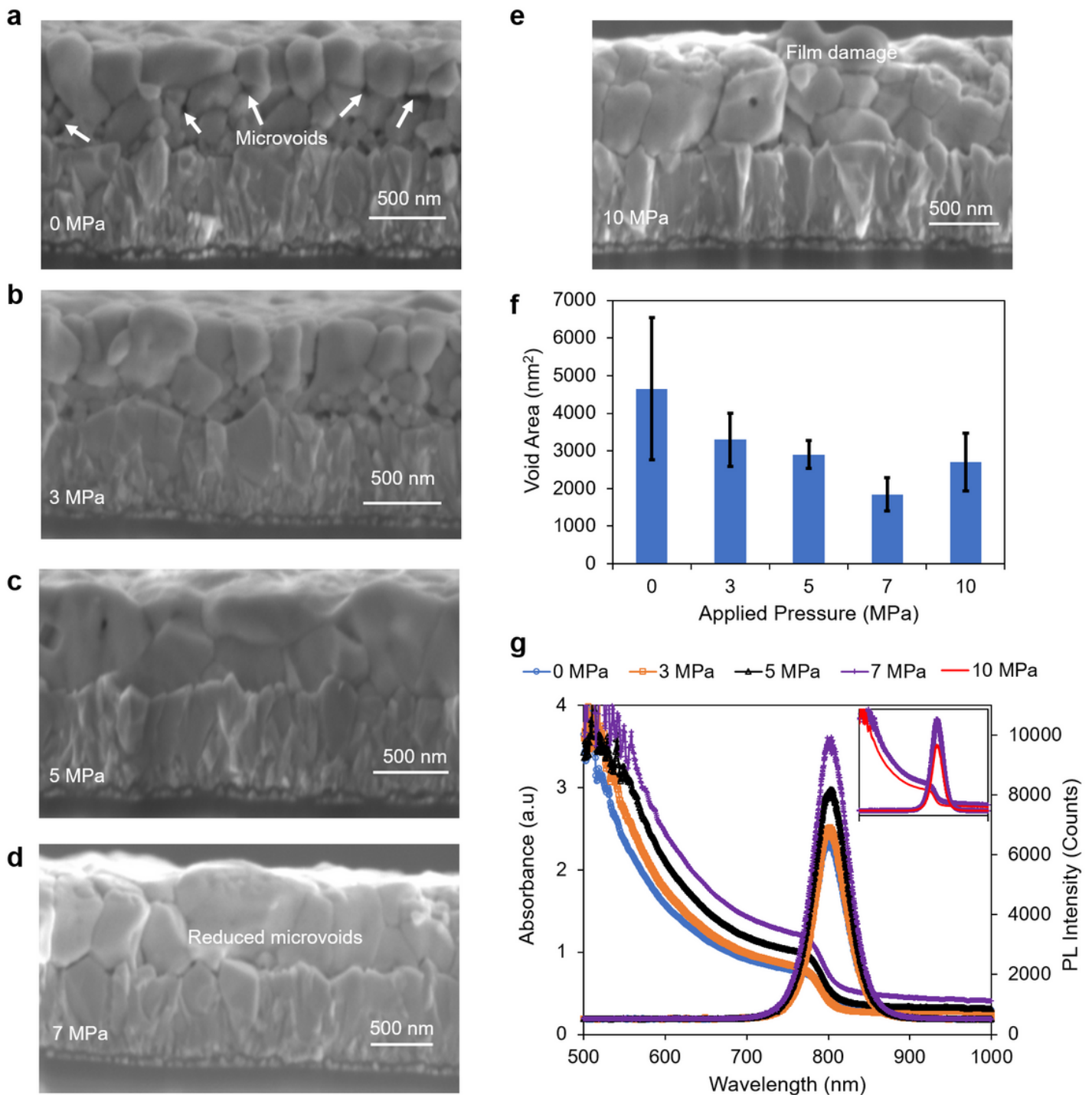


Figure 7

Pressure effects on multilayer defects and optical properties. (a-e) Cross-sectional SEM images of multilayer films at different applied pressures: 0 MPa, 3 MPa, 5 MPa, 7 MPa, and 10 MPa. (f) Area of the grain-boundary voids in the film for different applied pressures. (g) Optical absorbance and PL spectra of the films at different applied pressures between 0 – 7 MPa, with an inset that compares the absorbance and PL spectra of films assisted with pressures of 7 MPa and 10 MPa. Both void area and optical properties change in response to pressure.

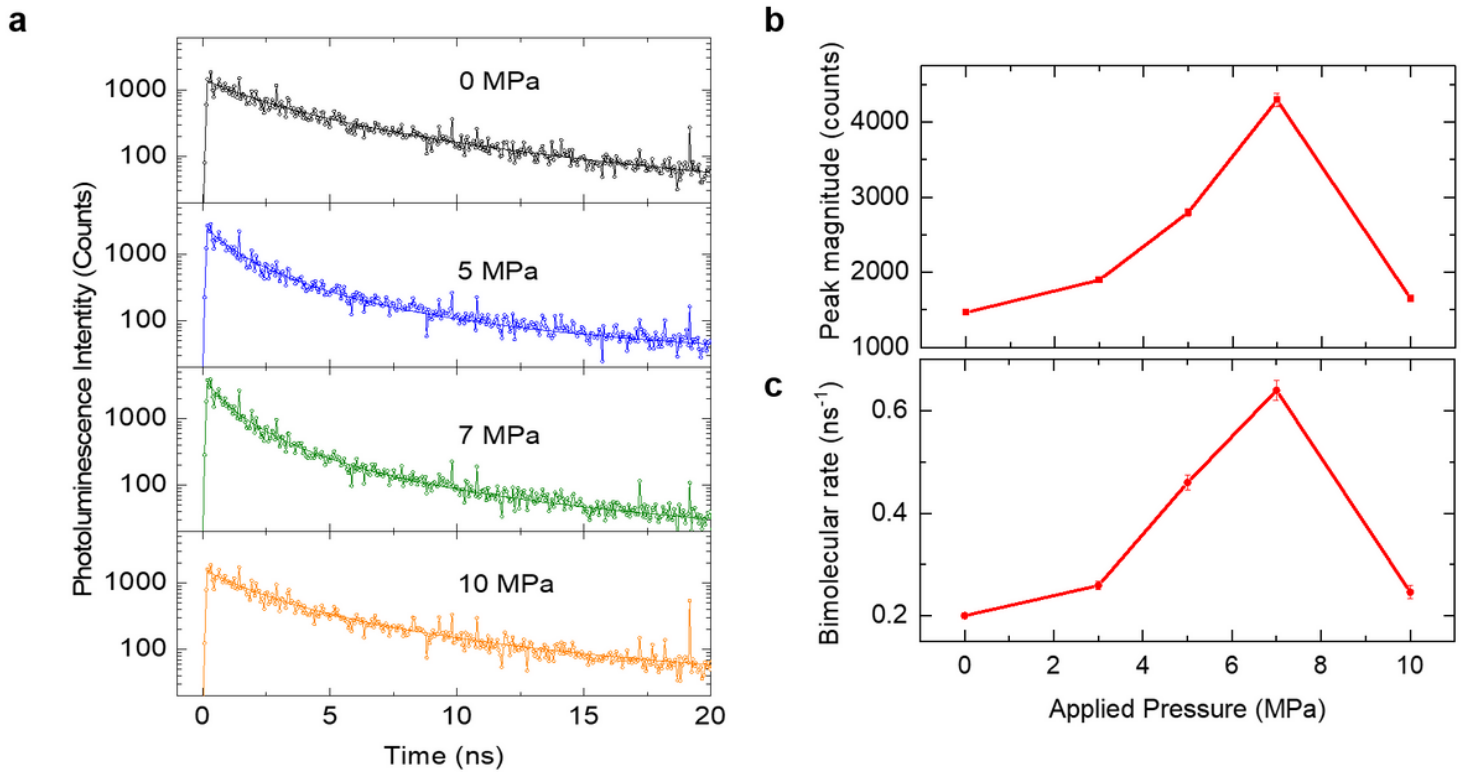


Figure 8

Effects of pressure on time-resolved photoluminescence (TRPL) of perovskite films: (a) TRPL decays of the perovskite multilayer films as a function of pressure applied during preparation, excited by a 485 nm pulse laser. Solid lines are fits to bimolecular recombination function. (b) Peak magnitude (I_0) from TRPL-decay fitting. (c) Bimolecular recombination rate (α) from TRPL-decay fitting. The data indicate fewer defects after applied pressures of 3 – 7 MPa.